Supplementary Information (SI) for Energy & Environmental Science.

Supplementary Information

Advancing High-Efficiency, Stretchable Organic Solar Cells: Novel Liquid Metal Electrode Architecture

Seungbok Lee,‡[a] Sungjun Oh,‡[a] Seungseok Han,‡[a] Dongchan Lee,[b] Jihyung Lee,[a] Yonghwi Kim,[c] Hoe-Yeon Jeong,[d] Jin-Woo Lee,[e] Min-Ho Lee,[a] Wu Bin Ying,[a] Seonju Jeong,[a] Seungjae Lee,[a] Junho Kim,[a] Yun Hoo Kim,[a] Bumjoom J. Kim,[e] Eun-chae Jeon,[d] Taek-Soo Kim,[c] Shinuk Cho[b] and Jung-Yong Lee*[a]

[a] School of Electrical Engineering, Korea Advanced Institute of Science and Technology (KAIST), Daejeon 34141, Republic of Korea

[b] Department of Physics and EHSRC, University of Ulsan, Ulsan 44610, Republic of Korea

[c] Department of Mechanical Engineering, Korea Advanced Institute of Science and Technology (KAIST), Daejeon 34141, Republic of Korea

[d] School of Materials Science and Engineering, University of Ulsan, Ulsan 44776, Republic of Korea

[e] Department of Chemical and Biomolecular Engineering, Korea Advanced Institute of Science and Technology (KAIST), Daejeon 34141, Republic of Korea

*All correspondence should be addressed to J.-Y.L. (email: jungyong.lee@kaist.ac.kr)

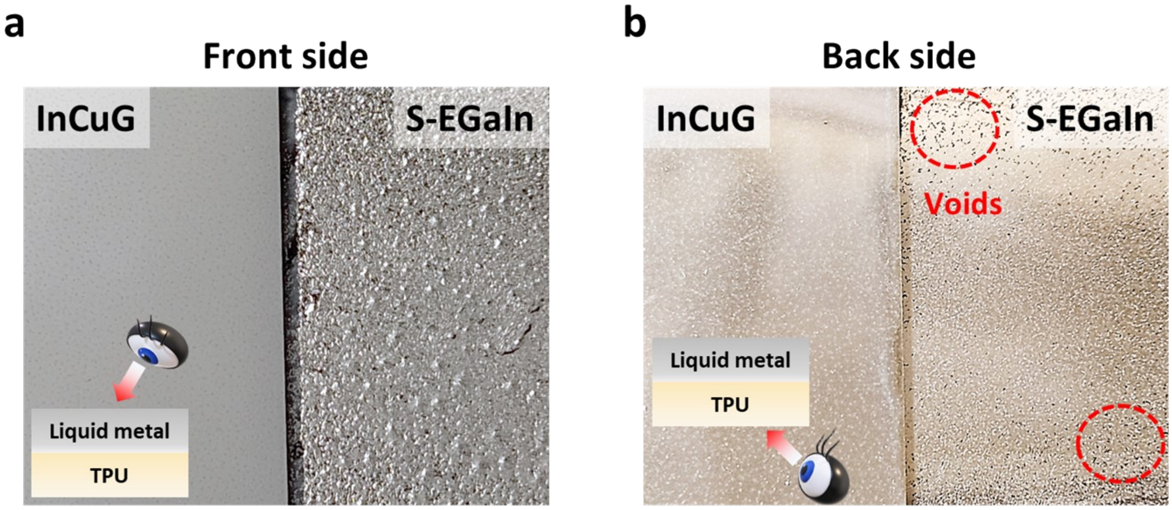

Figure S1. Photographs showing the a) front and b) back sides of the TPU/liquid metal film.

Figure S1 displays images of InCuG and S-EGaIn electrodes deposited on TPU substrates. In the front view, the InCuG electrode is characterized by its uniformity, smoothness, and superior resolution compared to the S-EGaIn electrode. The back side reveals that the InCuG electrode has a void-free appearance, whereas the S-EGaIn electrode displays numerous voids.

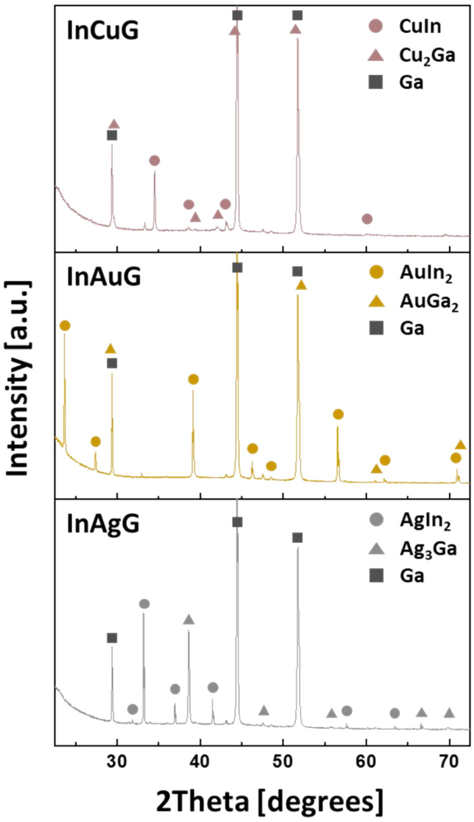

Figure S2. XRD patterns of InCuG, InAuG, and InAgG electrodes under -20°C and vacuum conditions.

Figure S2 represents the XRD patterns of InMiG electrodes deposited on TPU substrates. The peaks corresponding to In-Mi and Mi-Ga indicate that the InMiG electrodes were well-structured by the thermal evaporation process.

Table S1. International centre for diffraction data (ICDD) numbers of designated peaks.

Peak	ICDD Number
CuIn	00-035-1150
Cu_2Ga	01-078-8025
$AuIn_2$	03-065-8622
$AuGa_2$	01-073-2886
$AgIn_2$	03-065-1552
Ag_3Ga	00-051-1009
Ag_3GaO	00-073-0975
Ga	01-078-4238, 01-089-2735

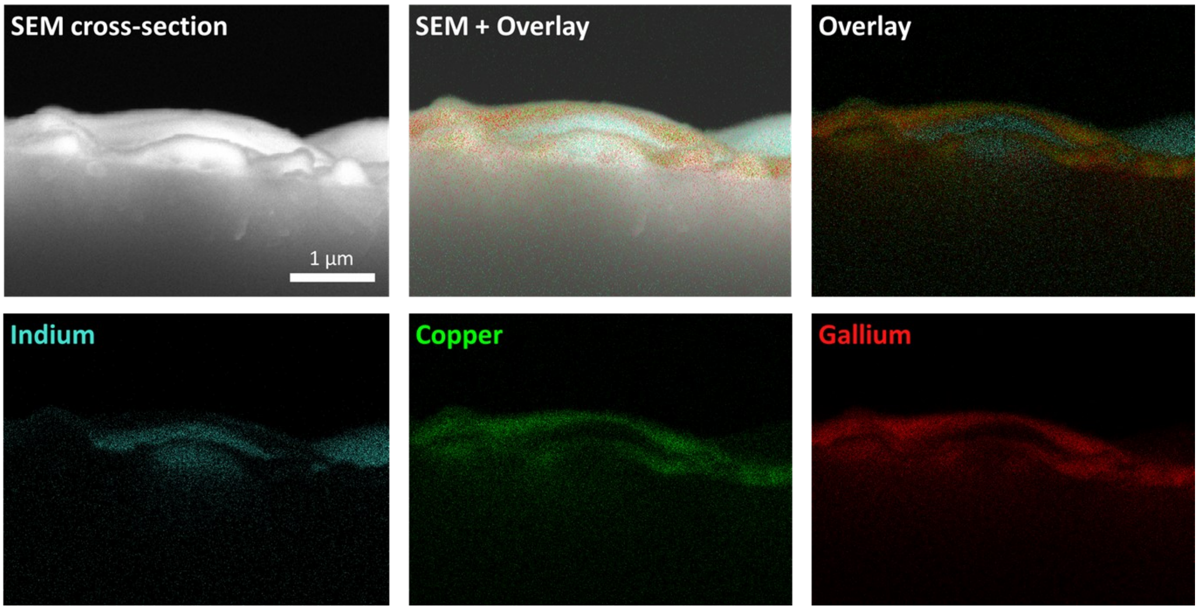

Figure S3. Cross-section SEM images of the InCuG electrode, along with the result of energy dispersive spectroscopy (EDS).

Figure S3 shows the cross-section images of the InCuG electrode, along with the elemental analysis results obtained through energy dispersive spectroscopy (EDS). As shown in the image, In is first deposited, followed by the sequential coverage of Cu and Ga.

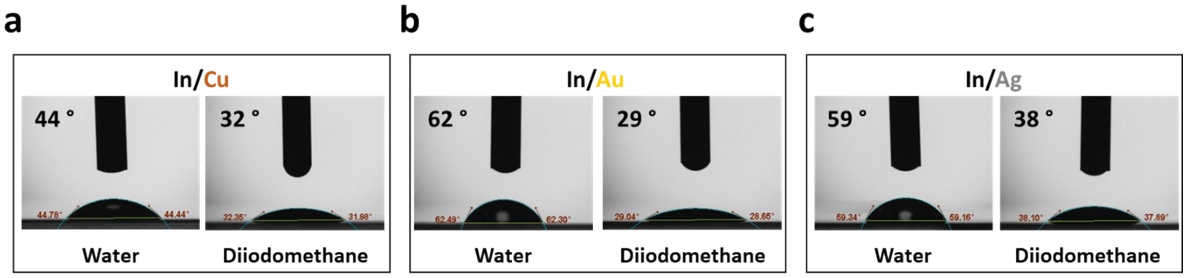

Figure S4. Contact angles of a) In/Cu, b) In/Au, and c) In/Ag with polar (deionized water) and nonpolar (diiodomethane) solvents.

Figure S4 represents the contact angles of TPU/In/metallic interlayers (Mi) using both polar and nonpolar solvents. Surface energies were calculated using Young's equation, where γ^d and γ^p represent dispersive and polar surface energy components, respectively, and γ_s is the total surface energy (Table S2). The In/Cu electrodes exhibited the highest surface energy among the three Mi candidates, suggesting that the Cu layer could enhance the wettability of Ga.

Table S2. Contact angle and surface energy of In/Mi films.

	Contact angle [°]		**Surface energy [mJ/m^2]**		
	Water	**Diiodomethane**	γ_S^d	γ_S^p	γ_S
In/Cu	44	32	31.8	25.7	57.5
In/Au	62	29	37.0	12.1	49.1
In/Ag	59	38	31.9	16.0	47.9

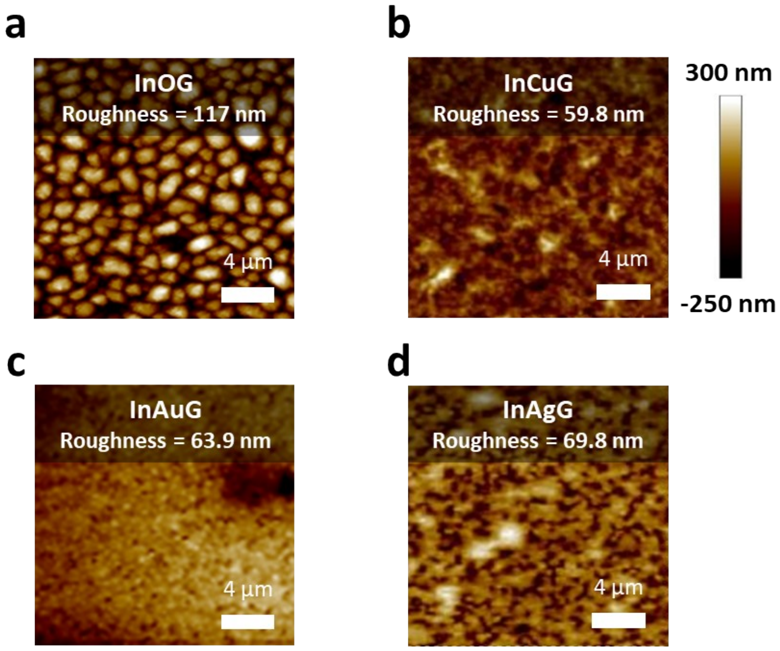

Figure S5. AFM images of a) InOG, b) InCuG, c) InAuG, and d) InAgG.

Figure S5 illustrates the surface roughness of liquid metal electrodes for different interlayer materials between In and Ga. It is particularly crucial for Ga to form as a thin film, as it can effectively fill in the gaps left by In, which might otherwise initiate cracks. Upon replacing the oxide layer with metallic interlayers, the surface roughness was significantly reduced from 117 nm (InOG) to 59.8 nm for InCuG, 63.9 nm for InAuG, and 69.8 nm for InAgG, suggesting that the Mi offers better wettability than the oxide layer. The lowest roughness achieved with the Cu interlayer is attributed to the highest surface energy of the In/Cu. These results were in good agreement with the trend in surface energy (Figure S4 and Table S2), suggesting that higher surface energy enhances Ga’s wetting properties, leading to the smoother and more uniform surfaces of InMiG electrodes.

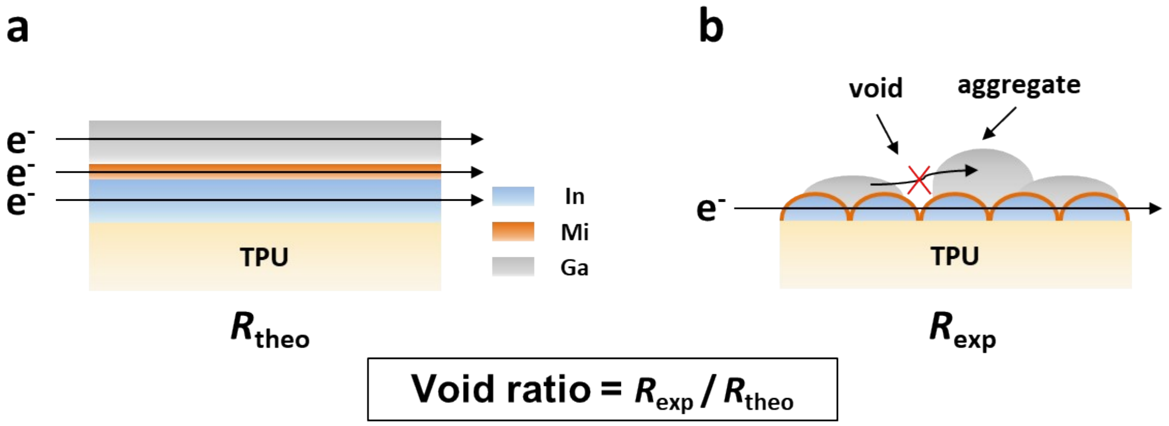

Figure S6. Schematic diagrams of a) ideal and b) nonideal (experimental) situations of liquid metal depositions.

Figure S6 illustrates a schematic of an InMiG electrode under both ideal and nonideal conditions. In the ideal scenario, each component forms a continuous thin film, resulting in optimal electrical performance without any loss. Conversely, in practical situations, In forms nanoclusters, followed by the deposition of Cu and Ga, and the presence of Ga clumps or voids within the electrodes is detrimental to electrical conductivity.

The void ratio is defined as the ratio of the experimentally measured sheet resistance (R_{exp}) of the electrode to its theoretically calculated sheet resistance (R_{theo}) using the same materials. This ratio quantifies the electrical loss originating from the voids relative to the continuous bulk film. A void ratio of 1 implies no electrical loss due to bumpy clusters or voids, indicating an ideal and uniform thin film formation. To achieve optimal electrical characteristics, it is essential that the Ga layer is deposited in a manner that closely resembles a thin film without clusters or voids. Table S3 shows the void ratios of InMiG electrodes for various Mi materials.

Table S3. Void ratio of InMiG electrodes.

	R_{exp} [Ω/sq]	R_{theo} [Ω/sq]	Void ratio
InOG	40	0.166	240
InCuG	0.55	0.130	4.23
InAuG	0.90	0.139	6.47
InAgG	1.3	0.129	10.1

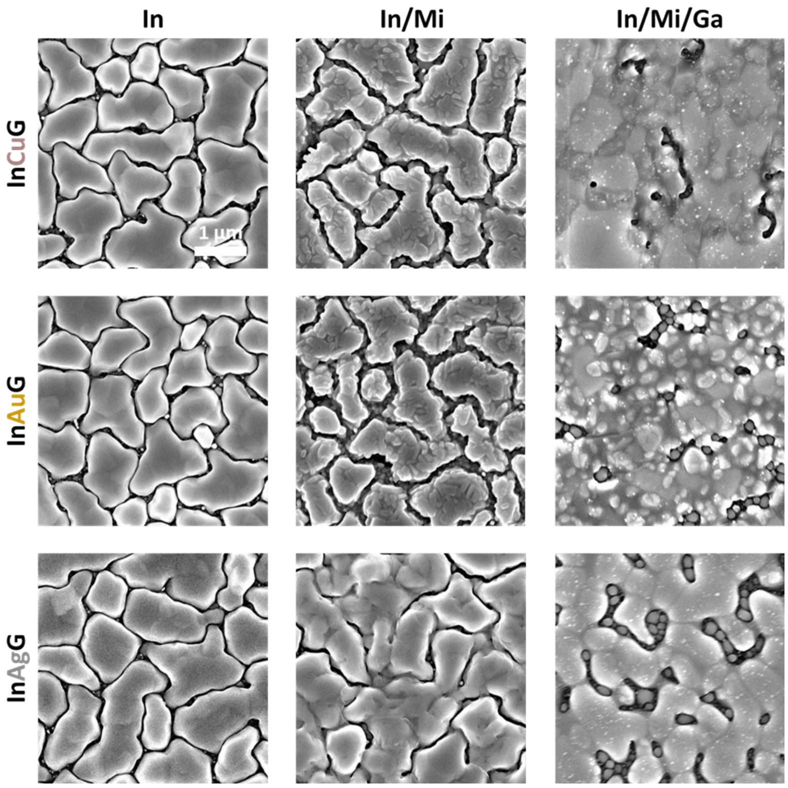

Figure S7. Scanning electron microscope (SEM) images of TPU/In, TPU/In/Mi, and TPU/In/Mi/Ga depending on various metallic interlayers.

Figure S7 illustrates the step-by-step formation process of the InMiG electrode as observed through SEM. A metallic interlayer (Mi) is deposited onto the In, altering the morphology. Subsequently, Ga is deposited onto the In/Mi structure, forming the stretchable electrode.

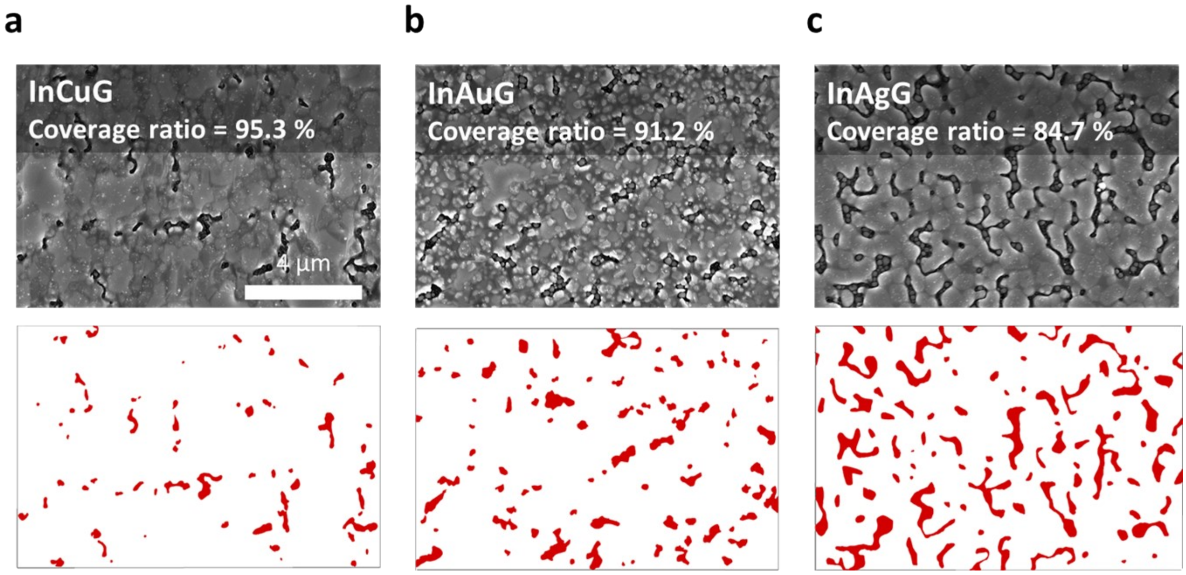

Figure S8. Surface coverage ratio of a) InCuG, b) InAuG, and c) InAgG electrodes. The surface coverage ratio was obtained from SEM images and calculated using the 'ImageJ' software.

Figure S8 shows the surface coverage ratio of InMiG electrodes for different types of Mi. A higher coverage ratio indicates complete coverage of the In/Mi structures by Ga. The thicknesses of In, Mi, and Ga were maintained at 400 nm, 30 nm, 170 nm, respectively. InCuG electrodes exhibited the highest surface coverage ratio at 95.3%, suggesting that Cu provides better wettability to Ga than other Mi.

In Figure 1f, the slope in the linear region from 50 to 100% strain was much lower for the InCuG electrode (1.26) compared to the InAuG (1.86) and InAgG (2.26) electrodes, which can be attributed to the presence of a continuous and well-covered Ga on the In/Mi structures, facilitated by the high surface energy of Cu (Figure 1d). When Ga thoroughly covers the underlying layers, it helps distribute stress effectively during stretching, thereby enhancing the mechanical robustness of the electrode[1-3]. For this reason, the resistance of the InCuG electrode also exhibited negligible changes up to 30% tensile strain.

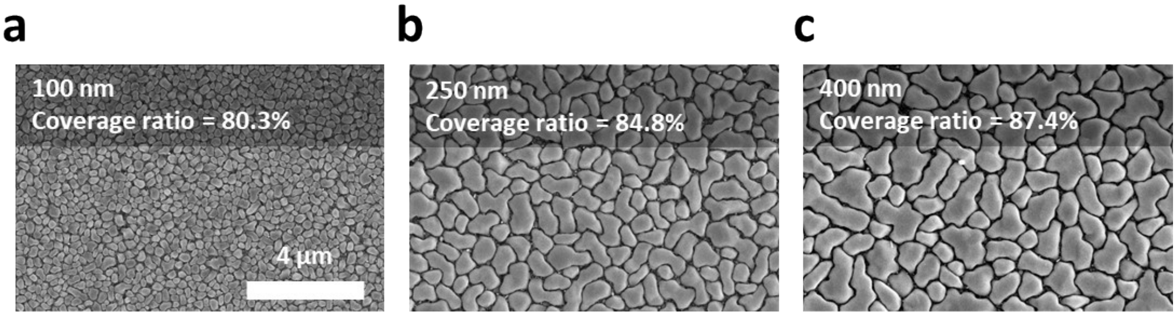

Figure S9. SEM images of In clusters at various thicknesses: a) 100, b) 250, and c) 400 nm.

Figure S9 depicts the morphology of In clusters as captured by SEM. As the thickness increases, the size of the In clusters also grows while maintaining 3D island structures consistent with the Volmer-Weber growth mode. Larger In clusters facilitate improved charge transport and reduce the void ratio, positively impacting the electrical properties (Table S4). In addition, the larger In clusters exhibit enhanced adhesion with the underlying layers due to a higher coverage ratio. This effectively distributes stress across the interface, thereby enhancing the mechanical properties.

Table S4. Electrical properties of InCuG electrodes as a function of the thickness of the In layer.

InCuG	R_{exp} [Ω/sq]	R_{theo} [Ω/sq]	Void ratio	Relative R @100% strain
100/30/170	1.80	0.24	7.50	4.64
250/30/170	1.20	0.17	7.06	3.70
400/30/170	0.55	0.13	4.23	1.90

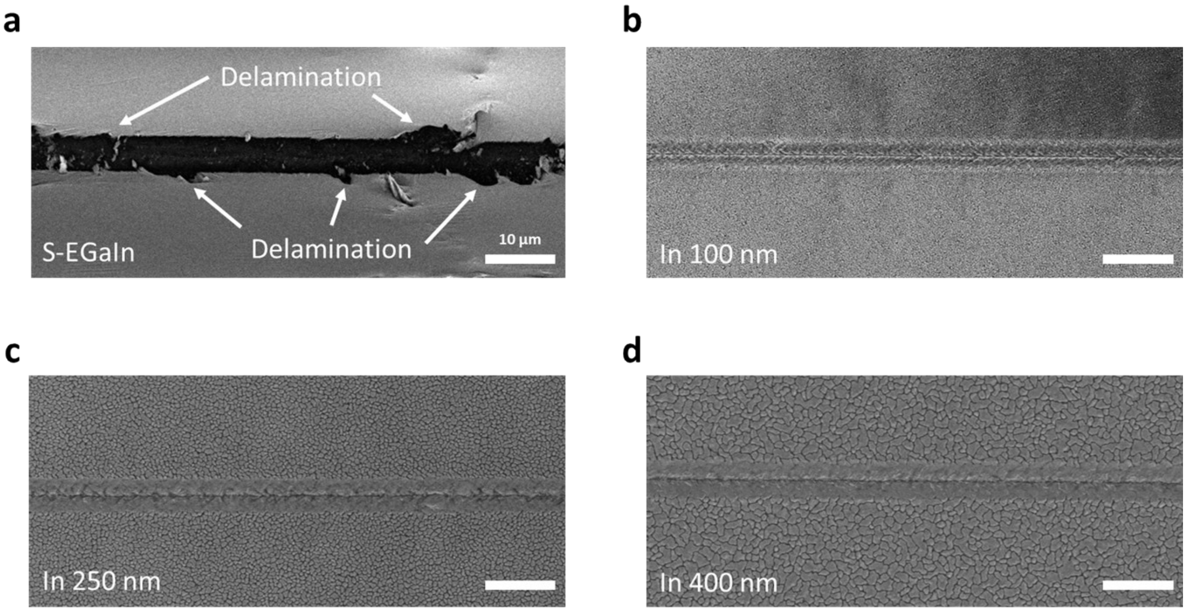

Figure S10. Pre-scan area of a) sprayed-EGaIn, and evaporated b) 100 nm, c) 250 nm, and d) 400 nm In on TPU substrate. Images were observed in top view.

Figure S10 represents the pre-scan scratch tracks resulting from the nano-scratch test on sprayed-EGaIn (S-EGaIn) and In layers with thicknesses of 100, 250, and 400 nm on a TPU substrate. Pre-scan is the process of scratching the surface of the specimen with the lowest vertical load of the machine (NST^3, Anton Paar), 0.5 mN, to account for the tilt of the specimen surface in determining the final indentation depth before conducting the main nano-scratch test. As shown in Figure S10a, delamination occurred in the S-EGaIn layer even under 0.5 mN, indicating poor adhesion between TPU and S-EGaIn. In contrast, even the 100 nm In layer (Figure S10b and Figure 2d), which exhibited the lowest adhesion among the In layers, did not show any delamination. This result demonstrates that S-EGaIn has significantly lower adhesion compared to the In layer, regardless of thickness.

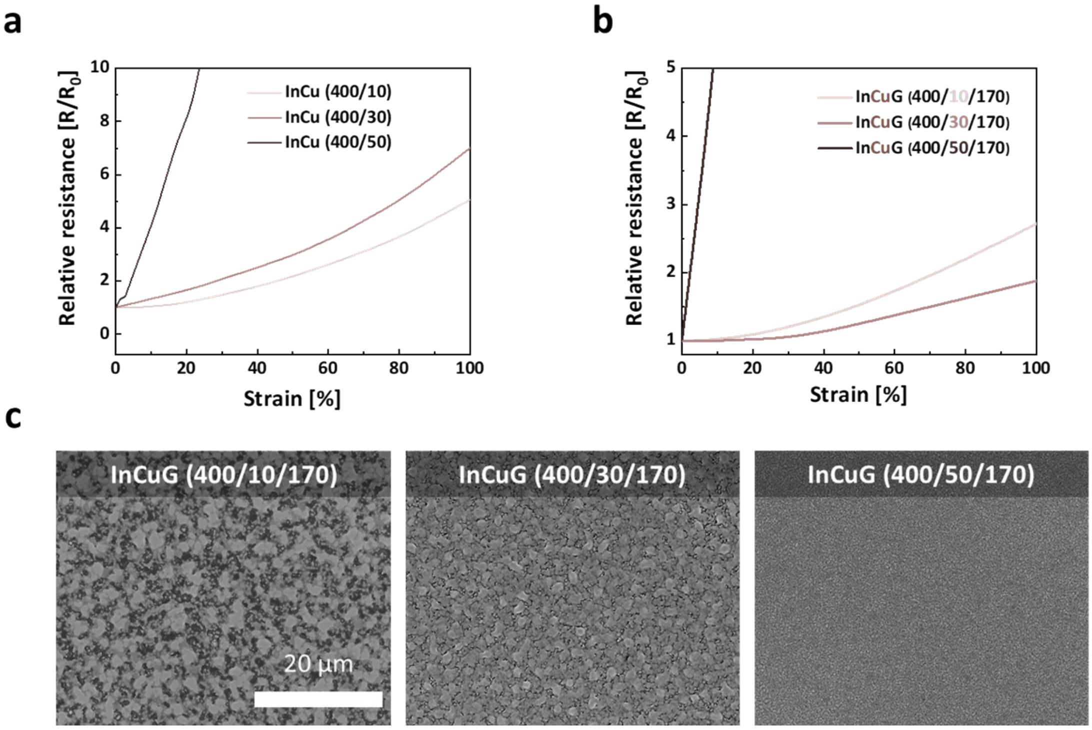

Figure S11. Analysis of Cu layer thickness effects on InCuG electrodes. Resistance changes of a) In/Cu and b) InCuG electrodes under tensile strain with varying copper layer thicknesses; c) SEM images of InCuG electrodes with 10, 30, and 50 nm thicknesses.

Figure S11 shows the influence of Cu thickness on the electrical and mechanical properties of InCuG electrodes. In Figure S11a, Cu layers ranging from 10 nm to 50 nm were deposited atop a 400 nm thick In layer. It was observed that thicker Cu layers detrimentally affect mechanical properties due to the inherent rigidity of Cu. However, a different trend emerged for InCuG electrodes as shown in Figure S11b, where the 30 nm Cu layer exhibited the most balanced mechanical properties, with only a 1.9-fold increase in resistance under 100% tensile strain.

Cu facilitates the wettability of Ga (Figure 1d), and therefore, as the thickness of the Cu layer increases, Ga can cover it more uniformly. Increasing the thickness of the Cu layer in InCuG electrodes from 10 to 50 nm resulted in reduced sheet resistance from 1.7 to 0.43 Ω/sq and void ratio from 11.3 to 3.91. However, because of the rigidity of the Cu layer, relative resistance under

100% strain drastically increases up to 77 (Table S5). Stretchability remained largely unaffected when the Cu layer thickness was between 10 and 30 nm, but it notably declined beyond a thickness of 30 nm, indicating that an overly thick metallic interlayer compromises stretchability due to increased rigidity.

SEM analysis further elucidates this paradox (Figure S11c). The InCuG electrodes with a 10 nm Cu layer showed numerous voids, indicating insufficient wettability by Ga on such a thin Cu layer, which deteriorates the mechanical properties. Conversely, increasing the Cu layer led to the formation of smoother and more uniform Ga films. Therefore, a 30 nm Cu layer was chosen as the optimal thickness, offering a balanced improvement in both electrical and mechanical properties.

Table S5. Electrical properties of InCuG electrodes as a function of the thickness of the Cu layer.

InCuG	**R_{exp} [Ω/sq]**	**R_{theo} [Ω/sq]**	**Void ratio**	**Relative R @100% strain**
400/10/170	1.70	0.15	11.3	2.7
400/30/170	0.55	0.13	4.23	1.9
400/50/170	0.43	0.11	3.91	77

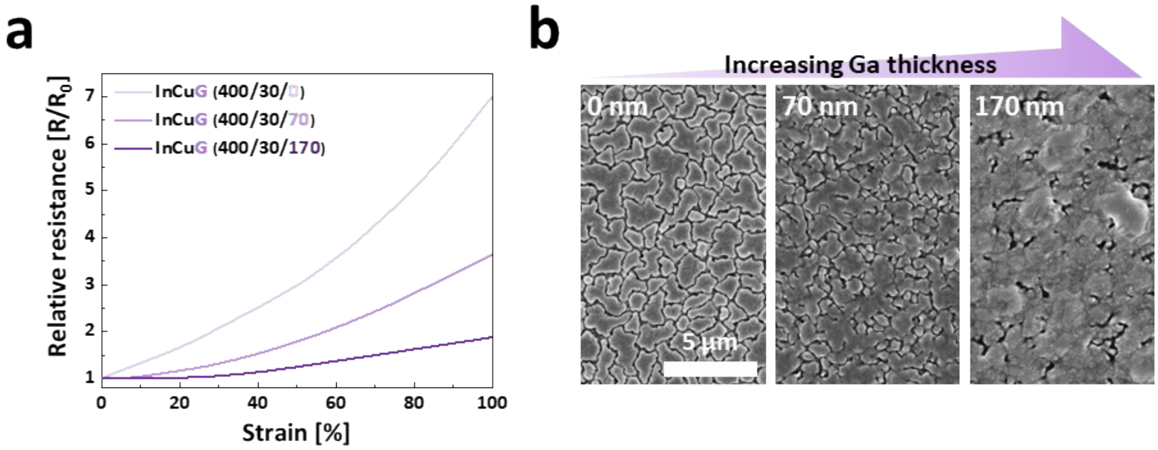

Figure S12. Analysis of Ga layer thickness effects on InCuG electrodes. a) Resistance changes of InCuG electrodes under tensile strain with varying Ga layer thicknesses; b) SEM images of InCuG electrodes with 0, 70, and 170 nm thicknesses.

Figure S12 shows the effect of Ga thickness on the electrical and mechanical properties of InCuG electrodes. As the thickness of Ga increased from 0 to 170 nm in InCuG electrodes, the sheet resistance decreased from 1.6 to 0.55 Ω/sq, and the void ratio decreased from 10.7 to 4.23, demonstrating effective coverage of the In/Cu electrodes by Ga (Table S6). It is imperative that Ga completely covers the In/Cu structure, as inadequate coverage can lead to stress concentration within the In/Cu, resulting in accelerated degradation. Under 100% strain, InCuG electrodes without a Ga layer (0 nm) exhibited a 7.0-fold increase in resistance (Figure S12a). However, the introduction of Ga in thicknesses ranging from 70 to 170 nm led to a reduction in relative resistance, decreasing from a 3.6- to a 1.9-fold increase. This trend suggests the importance of a smooth and uniform Ga layer in enhancing the stretchability of InCuG electrodes. Unlike the metallic interlayer, the stretchability of Ga reached a saturation point beyond 170 nm thickness. Therefore, 170 nm thick Ga layer was selected for InCuG electrodes.

Table S6. Electrical properties of InCuG electrodes as a function of the thickness of the Ga layer.

InCuG	R_{exp} [Ω/sq]	R_{theo} [Ω/sq]	Void ratio	Relative R @100% strain
400/30/0	1.60	0.15	10.7	7.01
400/30/70	1.10	0.14	7.86	3.66
400/30/170	0.55	0.13	4.23	1.90

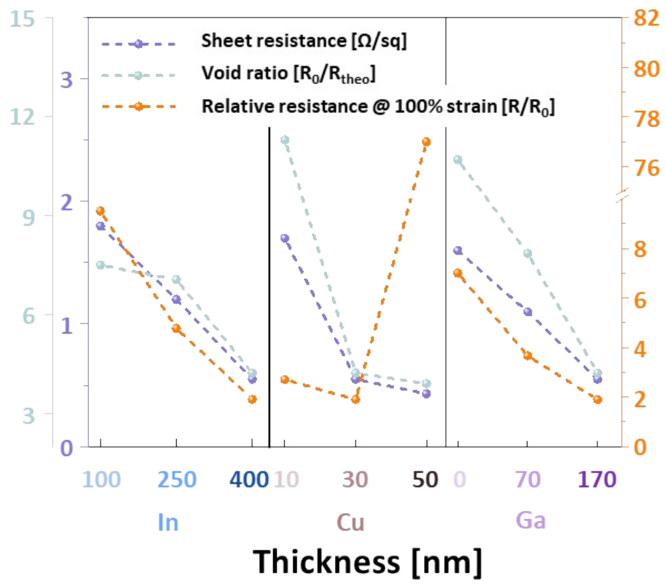

Figure S13. Comprehensive evaluation of the electrical properties of InCuG electrodes for different thicknesses of each constituent layer. The thicknesses of In, Cu, and Ga were maintained at 400 nm, 30 nm, and 170 nm, respectively, unless otherwise specified in the study.

Figure S13 represents the evaluation of the electrical properties of InCuG electrodes depending on the thicknesses of each layer. For In, the larger size of the clusters leads to better electrical and mechanical properties, therefore, 400 nm was adopted. Cu exhibits low sheet resistance at thicker thicknesses because they give enough wettability to Ga, yet compromises mechanical properties due to strengthened rigidity. Therefore, an optimal thickness of 30 nm was selected. Ga effectively covers the In/Cu structure as thickness increases, enhancing the sheet resistance and dissipating mechanical stress.

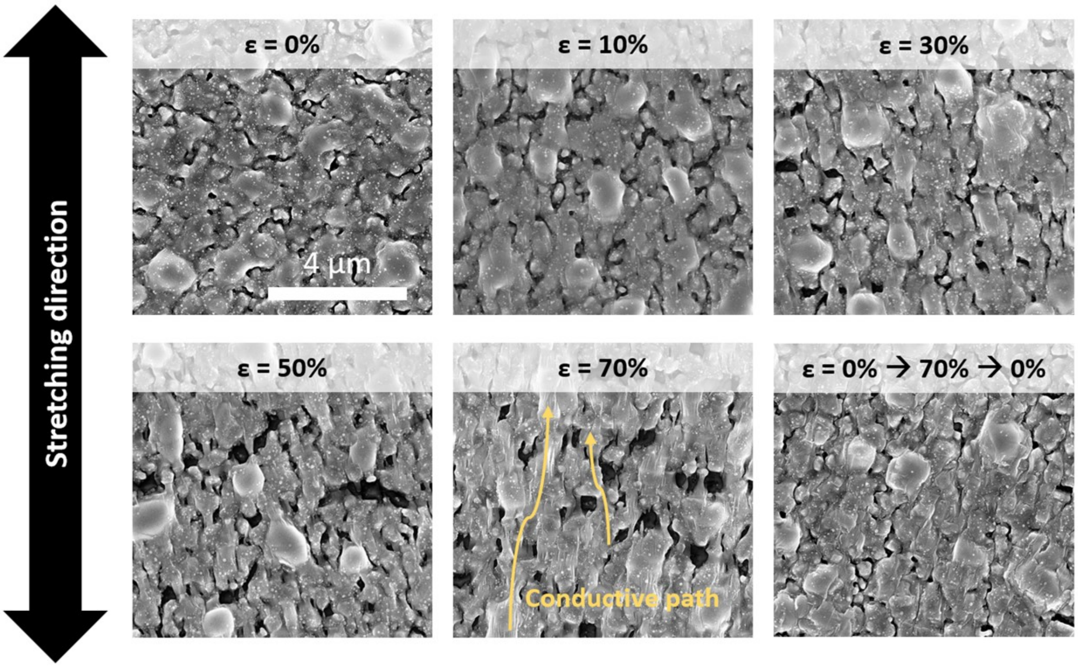

Figure S14. Scanning electron microscope (SEM) images of TPU/InCuG electrodes depending on tensile strains.

Figure S14 shows the in-situ SEM images of the TPU/InCuG electrodes under tensile strains. The InCuG electrodes exhibit continuous conductive pathways along the stretching direction, preserving their electrical properties under tensile strain. This result emphasizes the crucial role of stretchable substrates, as they dissipate applied stress while remaining stretchable[4]. It also underscores the importance of strong adhesion between indium and TPU substrate[5] (Figure 2d).

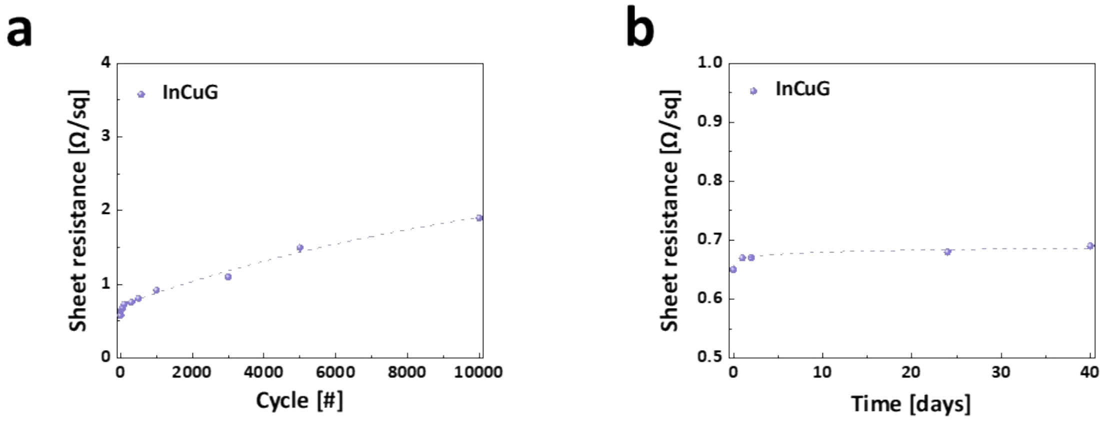

Figure S15. a) Mechanical stability assessment of InCuG electrodes under a 50% tensile strain; b) air stability for InCuG electrodes at room temperature with standard humidity (40% RH) conditions.

Long-term stability was evaluated through mechanical and air stability tests under ambient conditions. After 10,000 cycles at 50% strain, the sheet resistance modestly rose from 0.58 to 1.90 Ω/sq, suggesting promising potential for excellent stretchable electrodes. In the air stability tests, samples were stored at room temperature (25 °C) and 40% relative humidity for 40 days, during which the sheet resistance slightly increased from 0.65 to 0.69 Ω/sq, demonstrating excellent air stability.

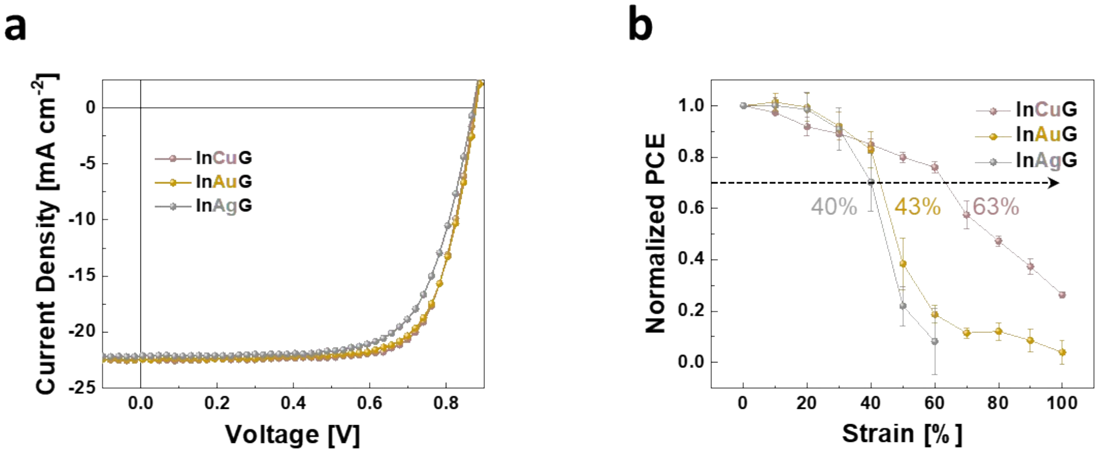

Figure S16. a) *J-V* characteristics for IS-OSCs with various metallic interlayers; b) Normalized PCE of IS-OSCs under tensile strains.

Figure S16 represents the electrical and mechanical performance of IS-OSCs based on different Mi. The InCuG-based IS-OSCs showed a superior *FF* (0.75), outperforming those based on InAuG (0.72) and InAgG (0.70) electrodes, attributed to their lower sheet resistance. Moreover, InCuG IS-OSCs achieved outstanding stretchability with an ε_{PCE70} of 63%, significantly surpassing the performance of IS-OSCs based on InAuG and InAgG. These results are consistent with TPU/InMiG experiments shown in Figures 1d-f. Therefore, InCuG electrodes were selected for the top electrode of IS-OSCs.

Table S7. Device performance metrics of IS-OSCs with various metallic-interlayers. The number represents the average values obtained from more than 10 samples.

	InCuG	**InAuG**	**InAgG**
V_{OC} [V]	0.87 (0.86)	0.87 (0.86)	0.86 (0.85)
J_{SC} [mA·cm^{-2}]	22.44 (22.19)	22.45 (22.19)	22.25 (21.46)
FF	0.75 (0.74)	0.72 (0.69)	0.70 (0.67)
PCE [%]	14.60 (13.98)	14.24 (13.35)	13.47 (12.19)
ε_{PCE70} [%]	63	43	40

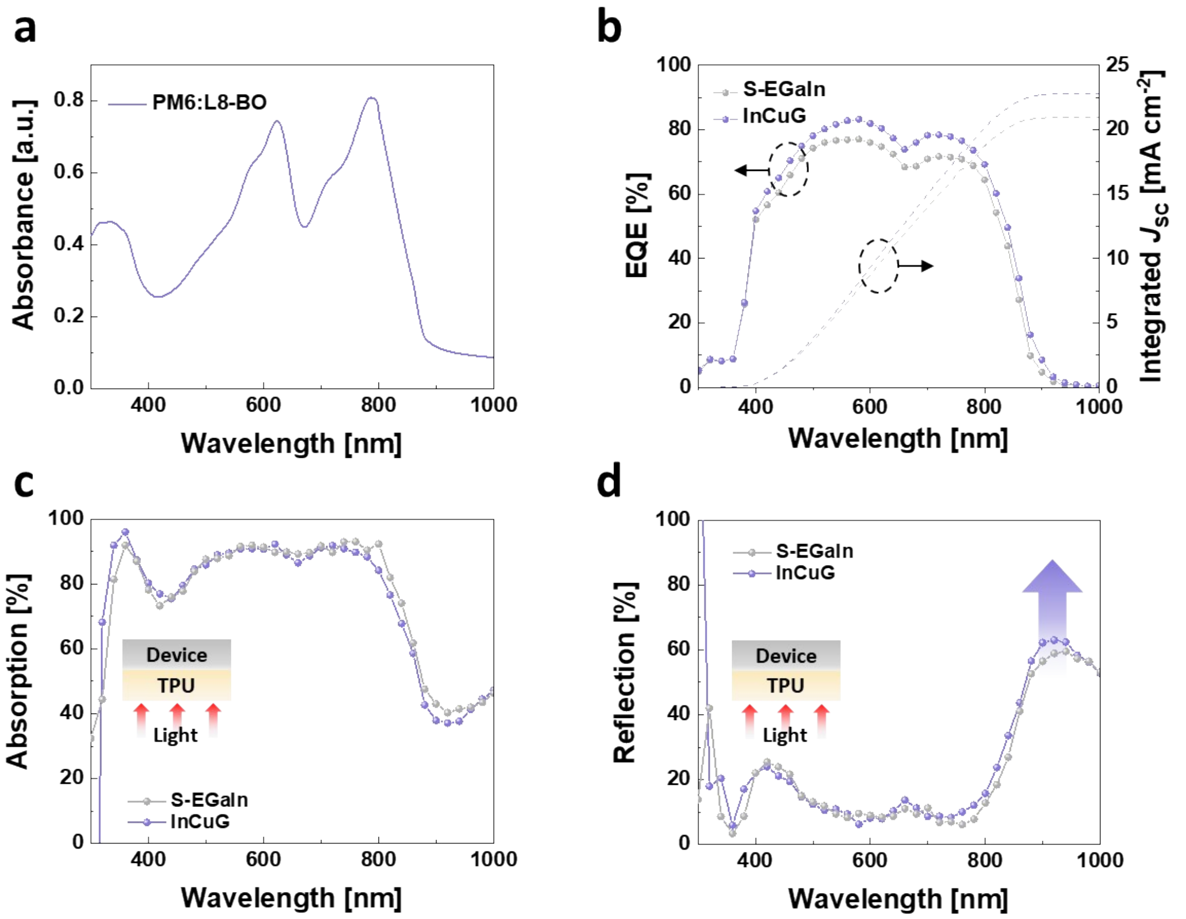

Figure S17. a) UV-vis absorption spectra of PM6:L8-BO blend; b) External quantum efficiency (EQE), c) absorption, and d) reflection spectra of IS-OSCs. The inset schematic illustrates the orientation and the direction of the measurements.

Figure S17a illustrates the absorption spectra of PM6:L8-BO bulk heterojunction (BHJ) blends used in this study. IS-OSCs were fabricated using PM6:L8-BO blends, and their external quantum efficiency (EQE) was measured with different stretchable top electrodes (Figure S17b). The calculated J_{SC} for InCuG-based IS-OSCs was 22.93 mA·cm^{-2}, exceeding that of S-EGaIn (21.08 mA·cm^{-2}). The calculated J_{SC} from EQE spectra demonstrated good agreement with the measured J_{SC} with a discrepancy of less than 4%. Interestingly, in the wavelength range of 700 to 950 nm, the absorption spectra of S-EGaIn IS-OSCs were slightly higher than those of InCuG IS-OSCs, deviating from the trend observed in EQE spectra (Figure S17c). This suggests the presence of parasitic absorption unique to the S-EGaIn electrodes in this specific wavelength region. Furthermore, the reflection spectra were analyzed to demonstrate the schematic depicted in Figure 3a (Figure S17d). The InCuG IS-OSCs exhibited enhanced reflection from wavelengths of 700 to 950 nm, suggesting that InCuG electrodes are characterized by a more uniform structure without any voids.

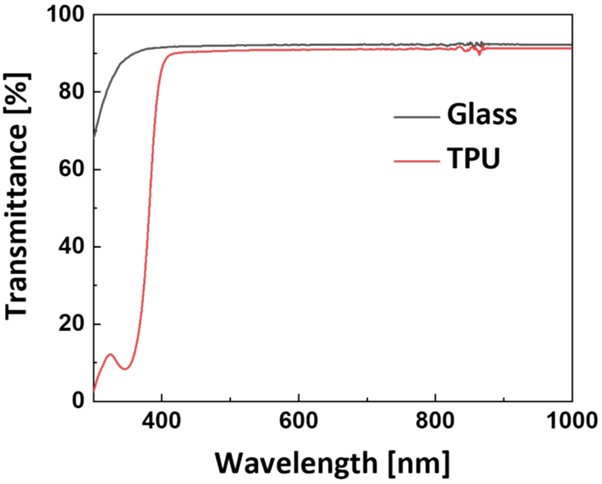

Figure S18. UV-vis transmittance of the glass and TPU substrate.

Figure S18 represents the UV-vis spectra of the glass and TPU substrates. The TPU substrate exhibits higher absorbance at wavelengths between 300 and 400 nm compared to glass, which hinders the light absorption of the active layer (Figure S17c). Additionally, the transmittance of the TPU (90.8%) is lower than glass (92.1%) at 550 nm wavelengths. Because of these inferior optical properties of the TPU substrate relative to glass, the current density of the TPU/PEDOT:PSS-based IS-OSCs is lower than that of glass/ITO-based OSCs (Figure S28).

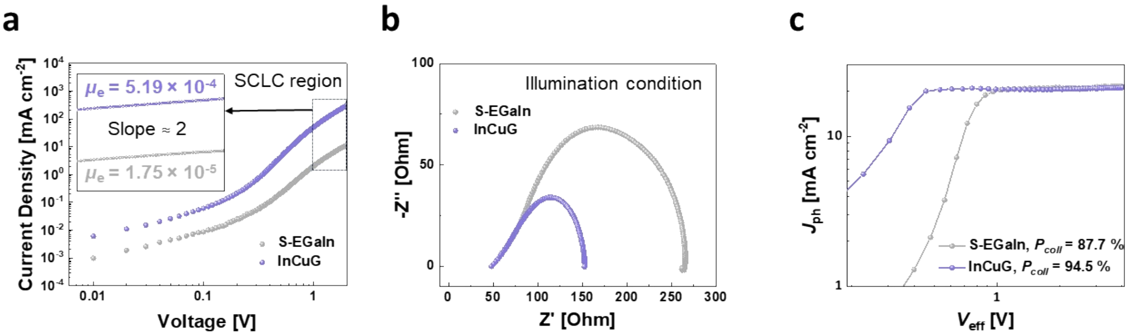

Figure S19. a) *J-V* characteristics for electron-only devices: TPU/PH1000/ZnO/PM6:L8-BO/PNDIT-F3N-Br/liquid metal. The inset graph represents the SCLC regime; b) Electrochemical impedance spectroscopy (EIS) measurements under illumination conditions; c) Photocurrent density versus effective voltage across IS-OSCs.

The charge dynamics within IS-OSCs were investigated, as shown in Figure S19. The space charge limited current (SCLC) was measured with electron-only devices to compare the electron mobility of IS-OSCs (Figure S19a). The InCuG IS-OSCs (5.19 × 10^{-4} cm^{2}V^{-1}s^{-1}) exhibited higher electron mobility compared to the S-EGaIn IS-OSCs (1.75 × 10^{-5} cm^{2}V^{-1}s^{-1}). These results could be attributed to the dense and uniform electrode formation of InCuG.

To further understand the charge transport mechanisms, EIS measurements were conducted under illumination at 0 V (Figure S19b). The results indicated that the charge transport resistance in InCuG IS-OSCs (47 Ω) is significantly lower than in S-EGaIn IS-OSCs (177 Ω), suggesting the superior charge transport capabilities of InCuG electrodes. Moreover, the charge collection efficiencies (P_{coll}) were calculated through photocurrent density versus effective voltage plots (Figure S19c). An effective voltage bias of up to 4 V was applied to ensure the complete extraction of photogenerated charge carriers[6, 7]. The P_{coll} of InCuG IS-OSCs (94.5%) exhibited better values than that of S-EGaIn (87.7%), showing a consistent trend with the SCLC and EIS analysis.

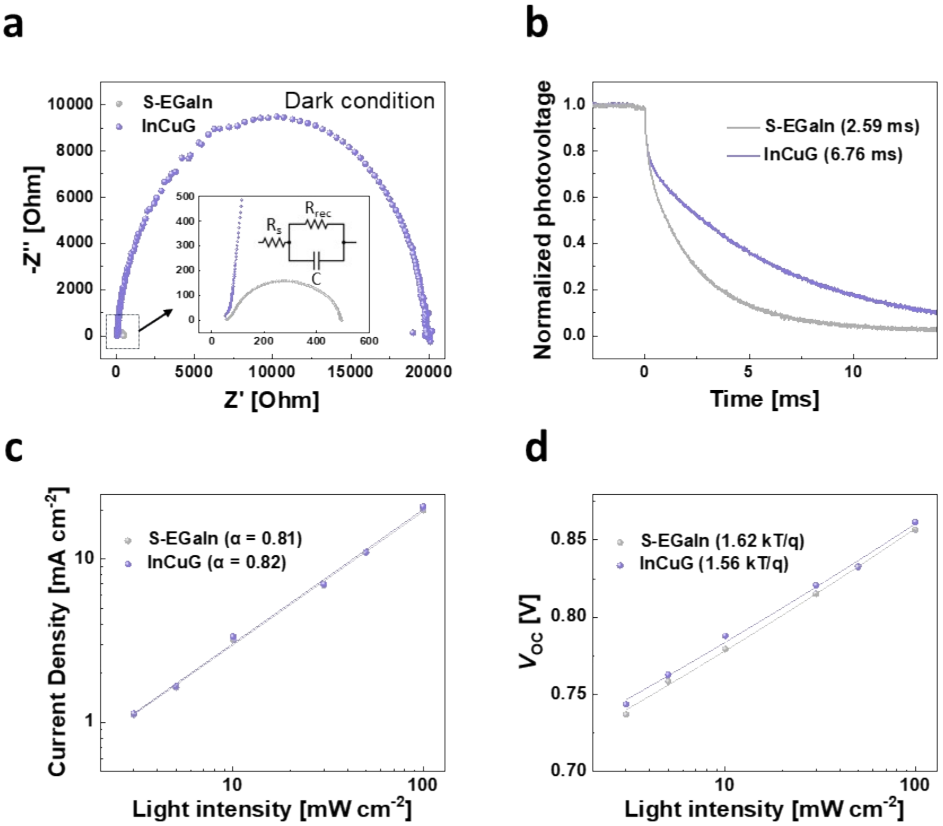

Figure S20. a) EIS data for IS-OSCs under dark conditions; b) Transient photovoltage (TPV) measurements of IS-OSCs depending on the top electrode deposition methods; Variation in c) J_{SC} and d) V_{OC} of IS-OCSs across a range of light intensities.

To investigate charge recombination dynamics, EIS under dark conditions was measured at a 0.8 V bias (Figure S20a). The charge recombination resistance of InCuG IS-OSCs greatly increased compared to S-EGaIn. These results imply that the charge carrier of InCuG based IS-OSCs were less prone to recombination.

Additionally, TPV measurements were performed to determine the carrier lifetimes within IS-OSCs (Figure S20b). The InCuG IS-OSCs exhibited a longer carrier lifetime (6.76 ms) than the S-EGaIn IS-OSCs (2.59 ms), indicating reduced recombination between the electron transport layer and the top electrode, an improvement attributed to the uniformly deposited InCuG electrodes.

Figure S20c presents the J_{SC} values across various light intensities, revealing negligible differences. This implies that bimolecular recombination is not a dominant factor in the observed recombination mechanisms. However, the slope of V_{OC} with respect to the light intensities indicates that trap-assisted recombination was alleviated when S-EGaIn electrodes were replaced with InCuG electrodes (Figure S20d).

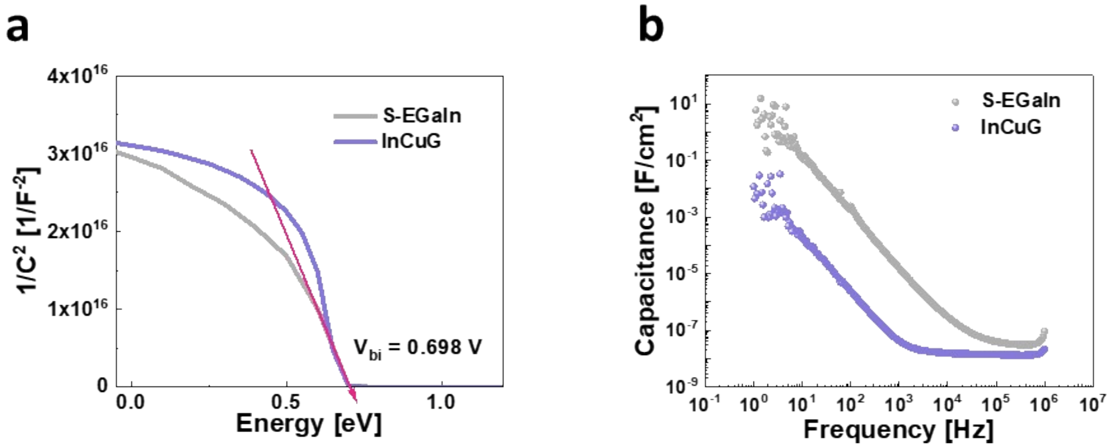

Figure S21. a) Mott-Schottky plot and b) frequency-dependent capacitance spectra of IS-OSCs.

To measure the trap density of states (tDOS) of IS-OSCs, the built-in potential (V_{bi}) was obtained through a Mott-Schottky plot (Figure S21a), using the following equation:

$$\text{tDOS} = -\frac{V_{bi}\,dC\ \ \omega}{qWd\omega k_BT}, \qquad (1)$$

where V_{bi} and W are built-in potential and depletion width, respectively, extracted from the Mott-Schottky plot. Additionally, q, C, ω, k_B, and T represent the elementary charge, capacitance, angular frequency, Boltzmann's constant, and temperature, respectively.

Given that both S-EGaIn and InCuG IS-OSCs utilized identical active layer composition (PM6:L8-BO), a consistent V_{bi} value of 0.698 V was obtained for both. Next, frequency-dependent capacitance was measured across a range of 1Hz to 1MHz (Figure S21b). The capacitance of S-EGaIn IS-OSCs was observed to be higher than that of InCuG IS-OSCs across all frequency regions. Using the obtained V_{bi} and frequency-dependent capacitance results, Figure 3e presents tDOS against E_ω, which is given by:

$$E_\omega = kTln\frac{\omega_0}{\omega} \qquad (2)$$

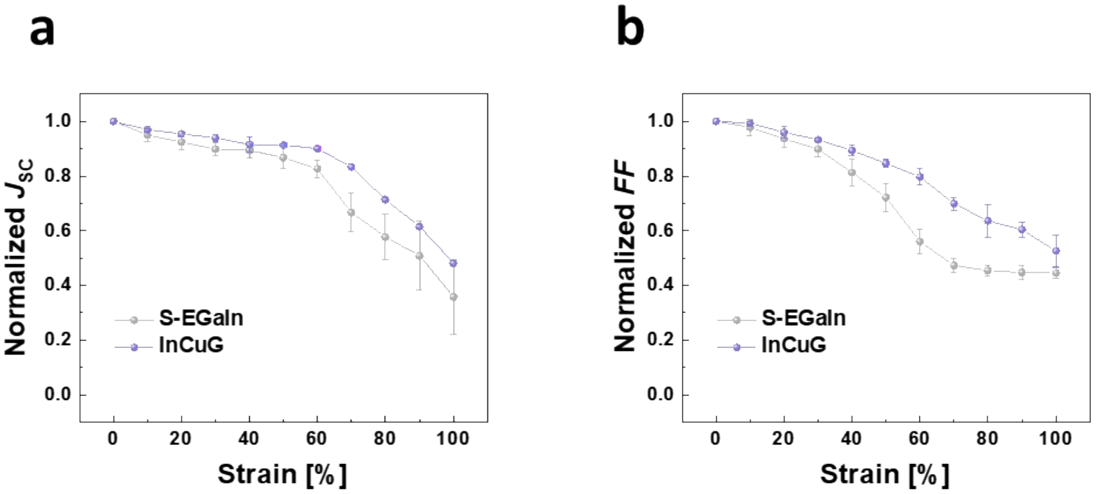

Figure S22. Normalized a) J_{SC} and b) *FF* of IS-OSCs under tensile strains.

Figure S22 represents the normalized performance parameters of IS-OSCs under tensile strains. InCuG IS-OSCs demonstrated a more gradual degradation compared to S-EGaIn IS-OSCs, indicating superior mechanical properties. The normalized J_{SC} results were in good agreement with the current density ratio data derived from OM images (Figure 4e).

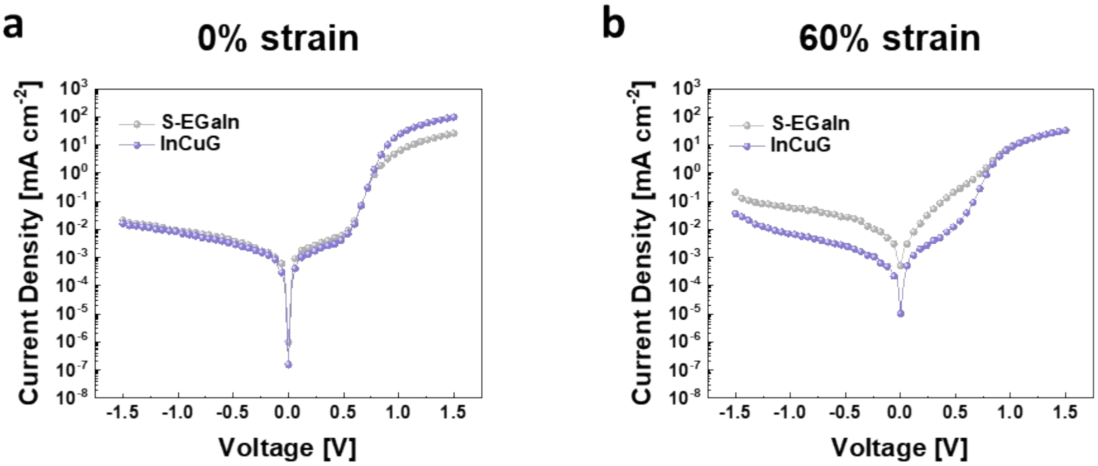

Figure S23. *J-V* characteristics of IS-OSCs with different top electrodes under dark conditions at a) 0% and b) 60% strain.

Figure S23 shows the *J-V* characteristics for IS-OSCs with different top electrodes under dark conditions. When subjected to 60% strain, the shunt resistance of S-EGaIn IS-OSCs experienced a substantial decrease from 46.4 to 6.88 kΩ cm^2 (85% drop). In contrast, InCuG IS-OSCs exhibited only a modest reduction in shunt resistance from 63.8 to 62.7 kΩ cm^2 (1.7% drop). This outcome suggests that InCuG electrodes enhanced mechanical and electrical resilience under stretching conditions.

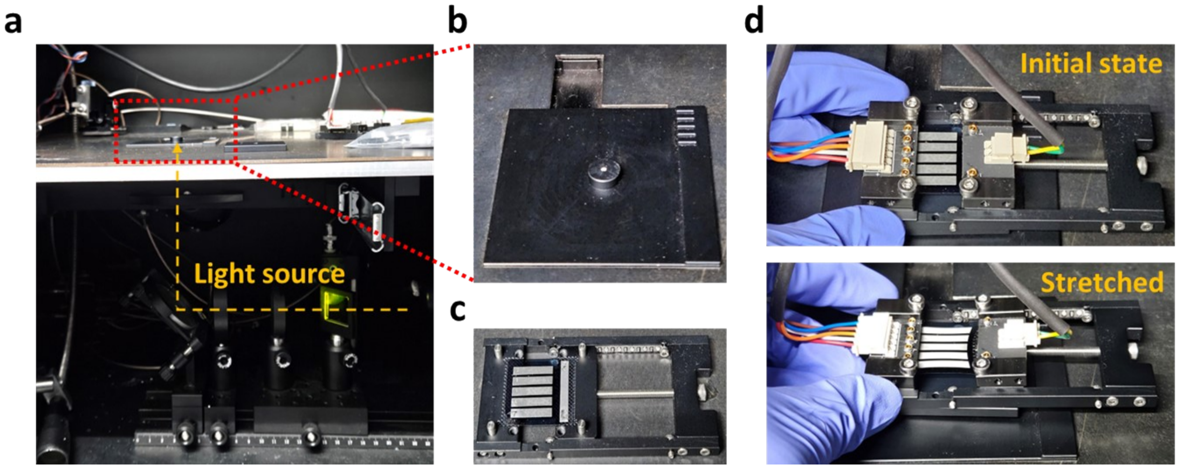

Figure S24. a) Photographs of measurement system for in-situ stretching EQE; b) a support to ensure that light is directed solely towards the sample; c) IS-OSCs with the stretchable jig before tightening; d) measurements before and after stretching.

Figure S24 shows the measurement system for in-situ stretching EQE. To avoid light scattering due to the distance between sample and light source, a custom support is designed to ensure that the light source is directed exclusively towards the sample. The measurements were conducted by positioning the device on a stretchable jig and characterizing it based on its tensile strain.

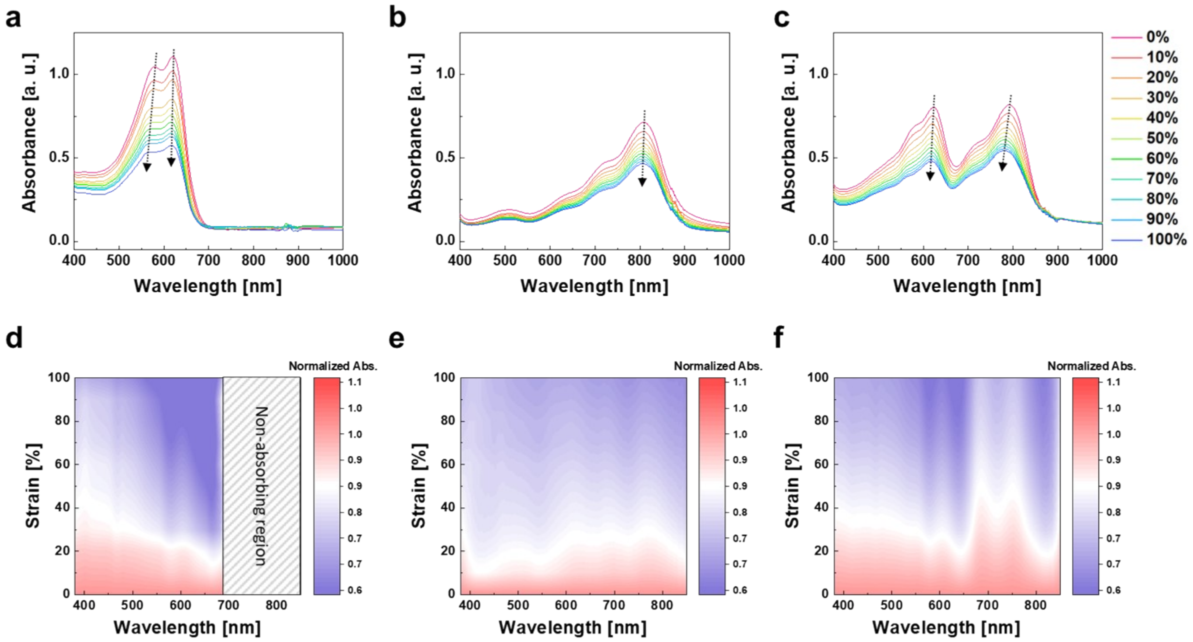

Figure S25. *In-situ* UV-vis spectra for a) PM6, b) L8-BO, and c) PM6:L8-BO blend films deposited on TPU; Normalized absorbance for d) PM6, e) L8-BO, and f) PM6:L8-BO blend films in response to applied strain.

Figure S25 presents *in-situ* UV-vis spectra of active layer films under varying tensile strains. Figures S25a-c depict the spectral changes for PM6, L8-BO, and PM6:L8-BO, respectively. Interestingly, the polymer donor, PM6, shows faster degradation under strain compared to the small-molecule acceptor, L8-BO. In the bulk heterojunction (BHJ) blend, the spectral range from 550 to 650 nm, corresponding to PM6, deteriorates more quickly than the range from 750 to 850 nm, which is attributed to L8-BO. To evaluate the spectral changes, the absorbance of each film was normalized to its initial value. Under 100% strain, PM6 showed a significant decrease in absorbance, with a 50% reduction (at 635 nm), while L8-BO films experienced a 35% drop (at 825 nm). Similarly, for BHJ films, the reductions were 43% at 635 nm and 37% at 825 nm under the same strain, indicating PM6's increased vulnerability, even within BHJ films. Although both PM6 and L8-BO show reduced absorption due to a reduction in thickness under tensile stress, the notable decrease in the absorption peak of PM6 can be primarily attributed to the disentanglement of its polymer chains[8-10]. Generally, polymers like PM6, due to their longer chain structure, have better stretchability than small molecules such as L8-BO. As a result, under tensile stress, PM6 can deform more effectively, resulting in a more pronounced reduction in absorption. This characteristic highlights the differential response of materials to mechanical stress based on their molecular structure. This trend is consistent with *in-situ* EQE results (Figure 4f).

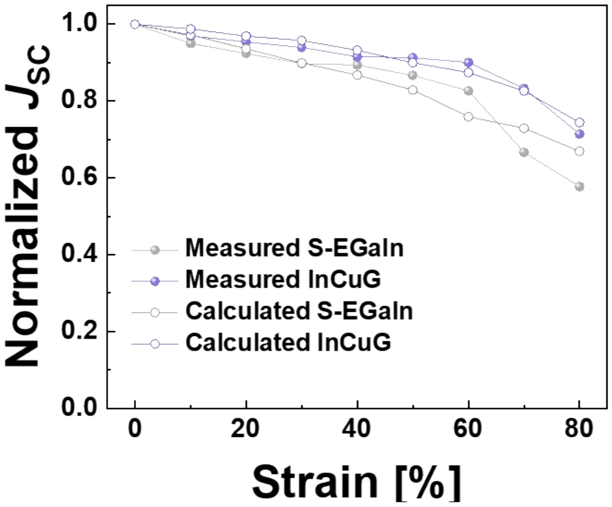

Figure S26. Normalized J_{SC} graph as a function of tensile strain, obtained from *J-V* curves and EQE measurements.

Figure S26 presents normalized J_{SC} values of InCuG and S-EGaIn IS-OSCs under tensile strains. The measured and calculated values were derived from *J-V* curves and EQE measurements, respectively. Both methods exhibited a similar tendency of decreased J_{SC}, indicating that stretching EQE measurement is reliable.

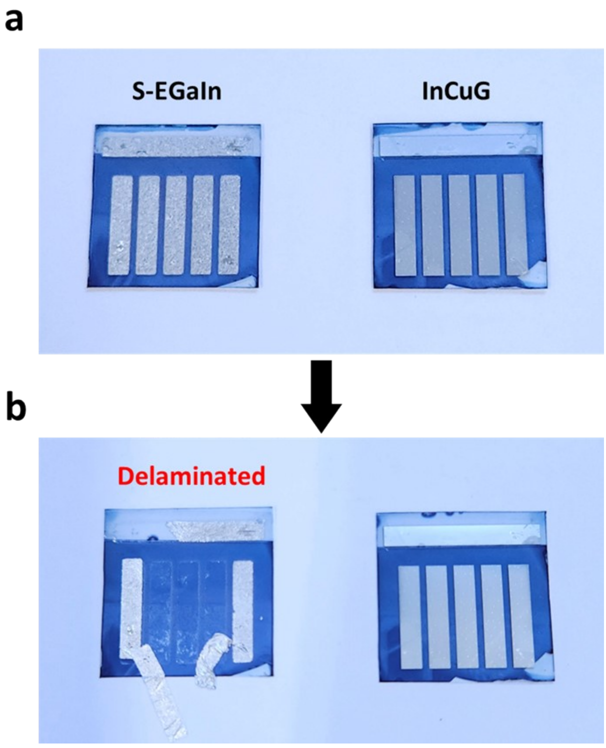

Figure S27. Photographs of IS-OSCs a) before and b) after immersion in liquid nitrogen.

Figure S27 displays the durability assessment of S-EGaIn and InCuG electrodes under extreme conditions. For this examination, IS-OSCs with these two different top electrodes were immersed in liquid nitrogen at -196 °C. The S-EGaIn electrodes exhibited a tendency for easy delamination, attributed to the higher thermal expansion forces acting between polymer layers and liquid metal surpassing the adhesion force. Meanwhile, the InCuG electrodes demonstrated robust adhesion, highlighting their excellent adhesion capabilities even under such extreme circumstances.

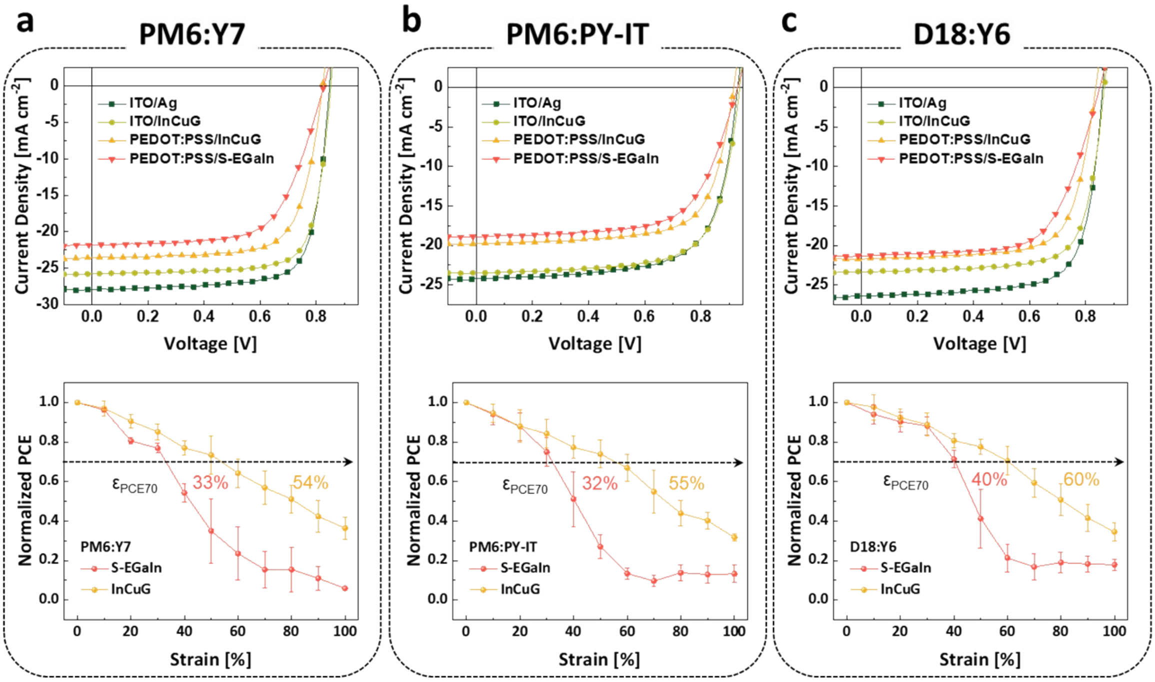

Figure S28. *J-V* characteristics and normalized PCEs under tensile strains of a) PM6:Y7, b) PM6:PY-IT, and c) D18:Y6-based OSCs.

Figure S28 shows the versatility of the InCuG electrodes on various active systems. To verify the compatibility of InCuG electrodes in OSCs, the performance was compared to that of Ag electrodes on glass/ITO substrates. All three types of active systems exhibited the same trend. The changes in open-circuit voltage (V_{OC}) and fill factor (*FF*) across the different electrodes were negligible. However, the short-circuit current density (J_{SC}) decreased after replacing Ag with InCuG, likely due to the lower reflectivity of In compared to Ag. Next, the bottom electrode was switched from ITO to PEDOT:PSS while retaining the InCuG electrode to fabricate IS-OSCs. The results indicated that the V_{OC}, J_{SC}, and *FF* decreased slightly in all three active systems. This decline is attributed to the reduced conductivity of PEDOT:PSS in comparison to ITO and the lower transmittance of TPU compared to glass (Figure S18). Finally, the top electrode was replaced with sprayed-EGaIn (S-EGaIn) while retaining the bottom electrode as PEDOT:PSS. Upon the introduction of the S-EGaIn electrode, both the J_{SC}, and *FF* decreased in all three active systems due to hindered charge extraction, as shown in

Figure 3d. This degradation can be attributed to the native oxide formed on EGaIn particles during spraying and the presence of numerous voids between the ETL and S-EGaIn interfaces (Figure 5b and Figure S1). These results are in good agreement with the PM6:L8-BO-based IS-OSCs.

Moreover, changes in PCE under tensile strain was examined to investigate the effect of InCuG electrodes on the mechanical performance of IS-OSCs. For IS-OSCs utilizing the S-EGaIn electrode, ε_{PCE70} values were 33%, 32%, and 40% for PM6:Y7, PM6:PY-IT, and D18:Y6, respectively. However, following the introduction of InCuG electrodes, the corresponding values increased by more than 20%, reaching 54%, 55%, and 60%, respectively. This result suggests that InCuG electrodes can be effectively applied to various high-efficiency organic solar cell systems and may serve as a powerful tool to simultaneously maximize efficiency and stretchability.

Table S8. Device performances of PM6:Y7-based OSCs depending on the various bottom and top electrodes. The data represent the average values obtained from more than 10 samples.

Bottom/Top electrode	V_{OC} [V]	J_{SC} [mA·cm^{-2}]	*FF*	PCE$_{max}$ (avg.) [%]	ε_{PCE70} [%]
ITO/Ag	0.85	27.90	0.76	17.98 (17.69)	-
ITO/InCuG	0.85	25.78	0.77	16.87 (15.95)	-
PEDOT:PSS/InCuG	0.82	23.58	0.72	14.06 (13.54)	54
PEDOT:PSS/S-EGaIn	0.83	21.79	0.65	11.79 (10.79)	33

Table S9. Device performances of PM6:PY-IT-based OSCs depending on the various bottom and top electrodes. The data represent the average values obtained from more than 10 samples.

Bottom/Top electrode	V_{OC} [V]	J_{SC} [mA·cm^{-2}]	*FF*	PCE$_{max}$ (avg.) [%]	ε_{PCE70} [%]
ITO/Ag	0.93	24.16	0.69	15.60 (15.22)	-
ITO/InCuG	0.94	23.44	0.71	15.52 (14.55)	-
PEDOT:PSS/InCuG	0.92	19.76	0.70	12.76 (12.23)	55
PEDOT:PSS/S-EGaIn	0.93	18.89	0.66	11.54 (10.28)	32

Table S10. Device performances of D18:Y6-based OSCs depending on the various bottom and top electrodes. The data represent the average values obtained from more than 10 samples.

Bottom/Top electrode	V_{OC} [V]	J_{SC} [mA·cm^{-2}]	*FF*	PCE$_{max}$ (avg.) [%]	ε_{PCE70} [%]
ITO/Ag	0.86	26.38	0.74	16.87 (16.48)	-
ITO/InCuG	0.87	23.32	0.74	15.02 (14.46)	-
PEDOT:PSS/InCuG	0.84	21.72	0.72	13.06 (12.36)	60
PEDOT:PSS/S-EGaIn	0.85	21.32	0.65	11.82 (10.82)	40

Table S11. Comparisons of the PCE and stretchability of IS-OSCs reported to date.

Year	Device structure	Active layer	PCE [%]	ε_{PCE70} [%]	*FF*	Ref.
2018	PDMS/PH1000/PEIE/Active layer/AI4083/EGaIn	P3HT:PCBM	1.00	44	-	[11]
2021	PDMS/PH1000/Active layer/EGaIn	PCE12:PCE10:N2200	6.43	15	0.56	[9]
2021	TPU/PH1000/AI4083/Active layer/PNDIT-F3N-Br/EGaIn	PM6:Y7	11.2	10	0.65	[4]
		PCE12:N2200	5.00	43	0.54	
2021	TPU/AgNW/PEDOT:PSS/Active layer/EGaIn	PCE10:IEICO-4F	10.1	13	0.63	[12]
2022	TPU/PH1000/AI4083/Active layer/PNDIT-F3N-Br/EGaIn	PM6:Y7:N2200	11.7	22	0.67	[13]
2022	TPU/PH1000/AI4083/Active layer/PNDIT-F3N/EGaIn	PM6:Y6	12.8	25	0.64	[14]
2022	TPU/PH1000/AI4083/Active layer/PNDIT-F3N-Br/EGaIn	PhAm5:Y7	12.73	34	0.70	[15]
2022	TPU/PH1000/AI4083/Active layer/PNDIT-F3N-Br/EGaIn	PM6-OEG5:BTP-eC9	12.05	24	0.69	[16]
2022	TPU/PH1000/AI4083/Active layer/PNDIT-F3N-Br/EGaIn	PBDB-T:PYFS-Reg	10.64	39	0.65	[17]
2023	TPU@AgNW/AI4083/Active layer/AZO@AgNW@AZO	PM6:BTP-eC9	10.9	12.5	0.66	[18]
2023	TPU/PH1000/AI4083/Active layer/PNDIT-F3N-Br/EGaIn	PM6:Y6-BO:N2200	10.2	44	0.62	[5]
		PCE12:N2200	6.20	70	0.65	
2023	TPU/PH1000/AI4083/Active layer/PNDIT-F3N-Br/EGaIn	PM7-Thy10:L8-BO	13.69	52	0.69	[19]
2024	TPU/PH1000/AI4083/Active layer/PNDIT-F3N-Br/EGaIn	D18$_{0.8}$-*s*-PEHDT$_{0.2}$:L8-BO	14.31	34.5	0.70	[20]
2024	TPU/PH1000/AI4083/Active layer/PNDIT-F3N-Br/EGaIn	D18:TYT-S	14.37	32.5	0.70	[10]
2024	TPU/PH1000/AI4083/Active layer/PNDIT-F3N-Br/EGaIn	PBQx-TF:DYBT-C4	14.25	38	0.70	[21]
2024	TPU/PH1000/AI4083/Active layer/PEI/PH1000/TPU	PBDB-T:N2200	4.00	42	0.59	[8]
2024	PU/PH1000/AI4083/Active layer/EGaIn	Ter-D18:Y6	14.18	63	0.67	[22]
2024	TPU/PH1000/AI4083/Active layer/PNDIT-F3N-Br/InMiG	PM6:L8-BO	14.6	63	0.75	***This Work***

Supplementary References

1. B. Persson, *Tribology Letters*, 2023, **71**, 66.
2. W. Cheng, P. F. Dunn and R. M. Brach, *The Journal of Adhesion*, 2002, **78**, 929-965.
3. M. Kılıç, E. Burdurlu, S. Aslan, S. Altun and Ö. Tümerdem, *Materials & Design*, 2009, **30**, 4580-4583.
4. J. Noh, G.-U. Kim, S. Han, S. J. Oh, Y. Jeon, D. Jeong, S. W. Kim, T.-S. Kim, B. J. Kim and J.-Y. Lee, *ACS Energy Letters*, 2021, **6**, 2512-2518.
5. S. Lee, Y. Jeon, S. Y. Lee, B. S. Ma, M. Song, D. Jeong, J. Jo, G. U. Kim, J. Lee, T. S. Kim, B. J. Kim and J.-Y. Lee, *Advanced Energy Materials*, 2023, **13**, 2300533.
6. L. Zhang, M. Zhang, Y. Ni, W. Xu, H. Zhou, S. Ke, H. Tian, S. Y. Jeong, H. Y. Woo, W.-Y. Wong, X. Ma and F. Zhang, *ACS Materials Letters*, 2024, **6**, 2964-2973.
7. H. Tian, Y. Ni, W. Zhang, Y. Xu, B. Zheng, S. Y. Jeong, S. Wu, Z. Ma, X. Du, X. Hao, H. Y. Woo, L. Huo, X. Ma and F. Zhang, *Energy & Environmental Science*, 2024, **17**, 5173-5182
8. Z. Wang, D. Zhang, M. Xu, J. Liu, J. He, L. Yang, Z. Li, Y. Gao, Y. Chen, H. Gong, L. Zhao, L.-Y. Zhang and M. Shao, *ACS Materials Letters*, 2024, **6**, 1811-1819.
9. Q. Zhu, J. Xue, L. Zhang, J. Wen, B. Lin, H. B. Naveed, Z. Bi, J. Xin, H. Zhao, C. Zhao, S. F. Liu and W. Ma, *Small*, 2021, **17**, 2007011.
10. J.-W. Lee, C. Sun, J. Lee, D. J. Kim, W. J. Kang, S. Lee, D. Kim, J. Park, T. N. L. Phan, Z. Tan, F. S. Kim, J.-Y. Lee, X. Bao, T.-S. Kim, Y.-H. Kim and B. J. Kim, *Advanced Energy Materials*, 2024, **14**, 2303872.
11. J. W. Mok, Z. Hu, C. Sun, I. Barth, R. Muñoz, J. Jackson, T. Terlier, K. G. Yager and R. Verduzco, *Chemistry of Materials*, 2018, **30**, 8314-8321.
12. Z. Wang, M. Xu, Z. Li, Y. Gao, L. Yang, D. Zhang and M. Shao, *Advanced Functional Materials*, 2021, **31**, 2103534.
13. J.-W. Lee, G.-U. Kim, D. J. Kim, Y. Jeon, S. Li, T. S. Kim, J. Y. Lee and B. J. Kim, *Advanced Energy Materials*, 2022, **12**, 2200887.
14. Z. Wang, D. Zhang, M. Xu, J. Liu, J. He, L. Yang, Z. Li, Y. Gao and M. Shao, *Small*, 2022, **18**, 2201589.
15. J.-W. Lee, S. Seo, S. W. Lee, G. U. Kim, S. Han, T. N. L. Phan, S. Lee, S. Li, T. S. Kim, J.-Y. Lee and B. J. Kim, *Advanced Materials*, 2022, **34**, 2207544.
16. J.-W. Lee, C. Lim, S. W. Lee, Y. Jeon, S. Lee, T. S. Kim, J.-Y. Lee and B. J. Kim, *Advanced Energy Materials*, 2022, **12**, 2202224.
17. J.-W. Lee, C. Sun, S.-W. Lee, G.-U. Kim, S. Li, C. Wang, T.-S. Kim, Y.-H. Kim and B. J. Kim, *Energy & Environmental Science*, 2022, **15**, 4672-4685.
18. J. Huang, Z. Lu, J. He, H. Hu, Q. Liang, K. Liu, Z. Ren, Y. Zhang, H. Yu, Z. Zheng and G. Li, *Energy & Environmental Science*, 2023, **16**, 1251-1263.
19. Q. Wan, S. Seo, S.-W. Lee, J. Lee, H. Jeon, T.-S. Kim, B. J. Kim and B. C. Thompson, *Journal of the American Chemical Society*, 2023, **145**, 11914-11920.
20. J.-W. Lee, H.-G. Lee, E. S. Oh, S.-W. Lee, T. N.-L. Phan, S. Li, T.-S. Kim and B. J. Kim, *Joule*, 2024, **8**, 204-223.
21. J.-W. Lee, C. Sun, S. Lee, D. J. Kim, E. S. Oh, T. N.-L. Phan, T. H.-Q. Nguyen, S. Seo, Z. Tan, M. J. Lee, J.-Y. Lee, X. Bao, T.-S. Kim, L. Changyeon, Y.-H. Kim and B. J. Kim, *Nano Energy*, 2024, **125**, 109541.
22. J. Wang, Y. Ochiai, N. Wu, K. Adachi, D. Inoue, D. Hashizume, D. Kong, N. Matsuhisa, T. Yokota, Q. Wu, W. Ma, L. Sun, S. Xiong, B. Du, W. Wang, C.-J. Shih, K. Tajima, T. Aida, K. Fukuda and T. Someya, *Nature Communications*, 2024, **15**, 4902.